Computational Mechanics
https://doi.org/10.1007/s00466-021-02035-z

ORIGINAL PAPER

A digital-twin and machine-learning framework for the design of multiobjective agrophotovoltaic solar farms

T. I. Zohdi[1]

Received: 2 March 2021 / Accepted: 10 May 2021

Abstract
This work develops a computational Digital-Twin framework to track and optimize the flow of solar power through complex, multipurpose, solar farm facilities, such as Agrophotovoltaic (APV) systems. APV systems symbiotically cohabitate power-generation facilities and agricultural production systems. In this work, solar power flow is rapidly computed with a reduced order model of Maxwell's equations, based on a high-frequency decomposition of the irradiance into multiple rays, which are propagated forward in time to ascertain multiple reflections and absorption for various source-system configurations, varying multi-panel inclination, panel refractive indices, sizes, shapes, heights, ground refractive properties, etc. The method allows for a solar installation to be tested from multiple source directions quickly and uses a genomic-based Machine-Learning Algorithm to optimize the system. This is particularly useful for planning of complex next-generation solar farm systems involving bifacial (double-sided) panelling, which are capable of capturing ground albedo reflection, exemplified by APV systems. Numerical examples are provided to illustrate the results, with the overall goal being to provide a computational framework to rapidly design and deploy complex APV systems.

Keywords Agrophotovoltaics · Digital-twin · Machine-learning

1 Introduction

Theoretically, if properly harnessed, solar energy is the most plentiful energy source available to society. A rough calculation (Fig. 1) to ascertain the amount of worldwide solar power available combines (a) The Earth's radius: $R \approx$ 6,400,000 m, (b) The Earth's surface area: $A \approx 4\pi R^2$, (c) The peak solar power per unit area: $p \approx$1300 Watts/m^2 and (d) The assumption that roughly $1/2$ of the Earth is illuminated at any given time and that, on average, the overall surface achieves $1/2$ peak illumination. This yields an estimate of $P = \frac{Ap}{4} \approx$167,358 terawatts. The actual number is approximately 173,000 terawatts (NREL [1]), which is still approximately 10,000 times the worldwide power usage in 2019. Solar power can be harnessed in a variety of ways (a) photovoltaics (largest use), (b) solar heating (primarily water heating), (c) solar-thermal technologies (using mirrors, concentrators and steam turbines), (d) molten salt technologies to store heat and redeploy to run steam turbines, (e) artificial photosynthesis (biomimicry of plants), etc. Photovoltaic systems are the most widely used solar conversion systems. They employ the semi-conducting materials that exhibit the photovoltaic effect. With dramatic price drops and readily available silicon, such systems have come to dominate solar energy conversion systems. The first practical solar cell was built in 1954 at Bell Labs, with the space industry being an early adopter, driven by power limitations in space for satellites. In the US alone, installed solar energy use has increased by a factor of 20 in the last decade. Issues around the technology now focus on large-scale deployment and integration with other societal infrastructure in urban and rural settings (NREL [1]), such as agricultural production systems. However, placement of such facilities has become increasingly harder in both urban and rural areas. *Next generation facilities need to be blended with other societal structures.* Such 'blended' systems are exemplified by Agrophotovoltaic (APV) systems, which symbiotically cohabitate power-generation facilities and agricultural production systems. APV systems have become increasingly popular to help reduce tensions between pure solar farms and large-scale agriculture over desirable land.

✉ T. I. Zohdi
zohdi@me.berkeley.edu

[1] Department of Mechanical Engineering 6117 Etcheverry Hall, University of California, Berkeley, CA 94720-1740, USA

Published online: 04 June 2021

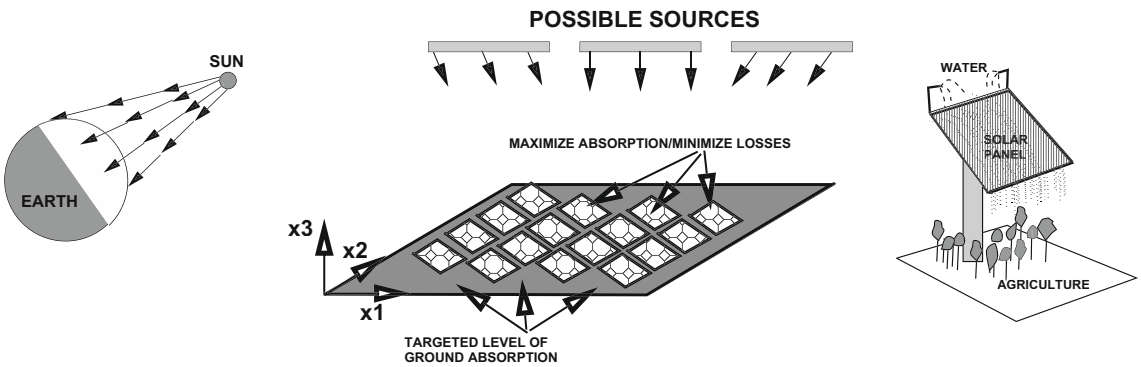

Fig. 1 Illumination of Earth for worldwide power estimates, an overall system and an APV unit

APV systems were pioneered in the 1980s (Goetzberger and Zastrow [2]) and have steadily grown as photovoltaic systems have become more robust and inexpensive. We refer the reader to [2–25] for a broad survey of such systems.[1] Regardless of the exact type of blended system, there is a necessity to optimize these complex multiobjective systems so that they operate properly. If configurations are properly optimized the approach can yield the best of both worlds, yielding energy and abundant agriculture. The approach allows for agricultural use of land in areas that would otherwise have been impossible to utilize. A common theme in these new paradigms is optimal system deployment. For a next generation solar farm designer, there are multiple surfaces to track, such the panel front, panel back, panel sides and the ground, and therefore a tool that keeps track of the absorption by each is advantageous. Accordingly, this work develops a computational Digital-Twin framework to track and optimize the flow of solar power through complex multipurpose solar farm facilities, such APV systems. Specifically, solar power flow is rapidly computed with a reduced order model of Maxwell's equations, based on a high-frequency decomposition of the irradiance into multiple rays, which are propagated forward in time to ascertain multiple reflections and absorption for various system configurations, varying multi-panel inclination, panel refractive indices, sizes, shapes, heights, ground refractive properties, etc. The method allows for a solar installation to be tested from multiple source directions quickly and uses a genomic-based Machine-Learning Algorithm to optimize the system. This is particularly useful for planning of complex next-generation solar farm systems involving bifacial (double-sided) panelling, which are capable of capturing ground albedo reflection, exemplified by APV systems (Fig. 1). A key to the presented approach is the 'Digital-Twin' paradigm of physical reality, i.e., digital replicas of complex systems that can then be inexpensively and safely manipulated, improved and optimized in a virtual setting. The system can then be deployed in the physical world afterwards, reducing the potential costs of experiments and accelerating development of new technologies. By creating Digital-Twins of complex, symbiotic APV systems, one can safely and efficiently manipulate, improve, and optimize agriculture, careful water use, and integrated solar energy in virtual settings, before deploying them in the physical world. We formulate a multiobjective optimization problem whose goal is to maximize power absorbed by the panels and which also simultaneously matches the power absorbed by the ground for agriculture. The approach can yield the best of both worlds, delivering energy and abundant agriculture. The approach allows planners to utilize and optimize land use in complex regions that would otherwise have been impossible.

[1] APV systems can involve a variety of aspects, even utilizing pollinating insects, such as bees, to 'solar grazing' systems.

2 Digital-twin structure and reduced-order model

2.1 Assumptions for reduced order model

The interest here is on the absorption of an initially (test) coherent pulse (Fig. 2), represented by multiple collimated (parallel) rays (initially forming a planar wave front), where each ray is a vector in the direction of the flow of power (the rays are parallel to the initial wave's propagation vector). We make the following observations:

- It is assumed that the features of the surface to be irradiated are at least an order of magnitude larger than the wavelength of the incident radiation (essentially specular (non-diffusive) optical surfaces), therefore "geometrical" ray tracing theory is applicable, and is well-suited for the systems of interest. It is important to emphasize the regimes of validity of such a model are where the surface features are larger than the optical wavelengths. For example, if we were to use rays (10^{-8} m $\leq \lambda \leq 4 \times 10^{-7}$ m), the features in this analysis would be assumed to possess scales larger than approximately

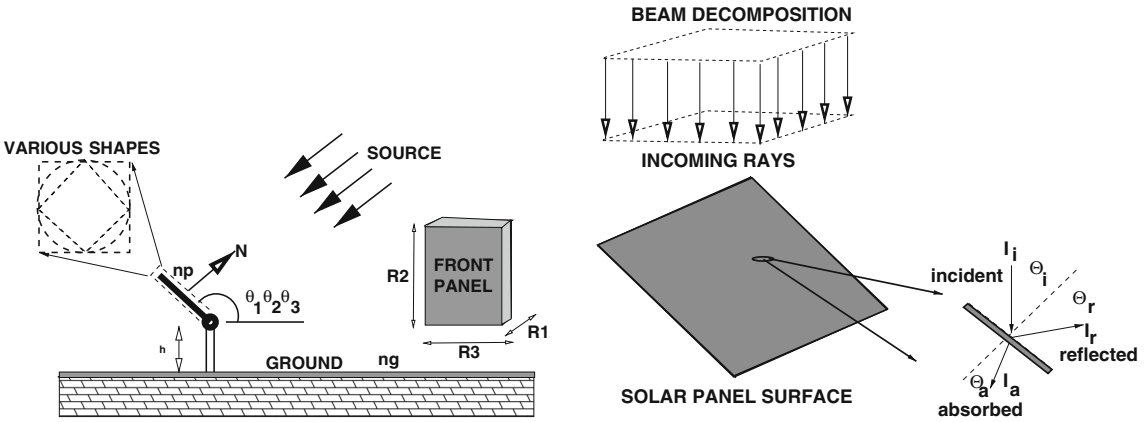

Fig. 2 Left: an overall system. Right: an electromagnetic pulse applied to a surface and a reduced order ray model

4×10^{-6} m. For systems containing features smaller than this, one can simply use the model as a qualitative guide.

- Ray-tracing is a method that is employed to produce rapid approximate solutions to wave-equations for high-frequency/small-wavelength applications where the primary interest is in the overall propagation of power.[2]
- Ray-tracing methods proceed by initially representing wave fronts by an array of discrete rays. *Thereafter, the problem becomes one of a primarily geometric character*, where one tracks the changing trajectories and magnitudes of individual rays which are dictated by the reflectivity and the Fresnel conditions (if a ray encounters a material interface).
- Ray-tracing methods are well-suited for computation of scattering in complex systems that are difficult to mesh/discretize, relative to procedures such as the Finite Difference Time Domain Method or the Finite Element Method.
- Other high frequency irradiation regimes can also be considered in the same manner, such as UV, X-rays and gamma rays, provided that the scattering target has the appropriate (larger) length-scale. Even in the case where this clear separation of length scales is not present, this model still provides valuable information on the propagation of the beam and the reflected response of the dispersed system.

Note the connection of the concept of a ray with a pulse/beam:

- We define $\bar{I}$ as the power per unit area, and we obtain the power of the entire pulse/beam by multiplying the irradiance by the cross-sectional area of an initially coherent beam, $\bar{I}A^b$, where A^b is the cross-sectional area of the beam (comprising all of the rays).
- The power for a ray in the pulse/beam is then given by $I = \bar{I}A^r = \bar{I}A^b/N_r$, where N_r is the number of rays in the beam (Fig. 2) and A^r can be considered the area associated with a ray.
- Fresnel reflection relations can then be used to compute changes in the magnitude of the reflected rays (and the amount absorbed), with directional changes given by the laws of reflection.

Essentially, rays are a mathematical construction/discretization of a pulse/beam. We refer the reader to Gross [26] and Zohdi [28–34] for details. From this point forth, we assume that the ambient medium behaves as a vacuum. Accordingly, there are no energetic losses as the rays move through the surrounding medium.

2.2 Reflection and absorption of rays

Following a framework found in Zohdi [28–34] for details, we consider a ray of light incident upon a material interface which produces a reflected ray and a transmitted/absorbed (refracted) ray (Fig. 2), the amount of incident electromagnetic power (I_i) that is reflected (I_r) is given by the total reflectance $\mathcal{IR} \stackrel{\text{def}}{=} \frac{I_r}{I_i}$, where $0 \leq \mathcal{IR} \leq 1$. The next section supplies the theory underpinning electromagnetic wave propagation and rays.

2.3 Electromagnetic wave propagation and rays

Following a framework found in Zohdi [28–34], the propagation of electromagnetic waves in free space can be described by a simplified form of Maxwell's equations (see Jackson [27], Zohdi [31])

$$\nabla \times \boldsymbol{E} = -\mu_o \frac{\partial \boldsymbol{H}}{\partial t}, \qquad \text{and} \qquad \nabla \times \boldsymbol{H} = \epsilon_o \frac{\partial \boldsymbol{E}}{\partial t}, \tag{1}$$

[2] Resolving diffraction (which ray theory is incapable of describing) is unimportant for the applications of interest.

where $\nabla \cdot \boldsymbol{H} = 0$, $\nabla \cdot \boldsymbol{E} = 0$, $\boldsymbol{E}$ is the electric field, $\boldsymbol{H}$ is the magnetic field, ϵ_o is the free space permittivity and μ_o is the free space permeability. Using standard vector identities, one can show that

$$\nabla \times (\nabla \times \boldsymbol{E}) = -\mu_o \epsilon_o \frac{\partial^2 \boldsymbol{E}}{\partial t^2}, \qquad \text{and}$$
$$\nabla \times (\nabla \times \boldsymbol{H}) = -\mu_o \epsilon_o \frac{\partial^2 \boldsymbol{H}}{\partial t^2}, \tag{2}$$

and that

$$\nabla^2 \boldsymbol{E} = \tfrac{1}{c^2} \tfrac{\partial^2 \boldsymbol{E}}{\partial t^2}, \qquad \text{and} \qquad \nabla^2 \boldsymbol{H} = \tfrac{1}{c^2} \tfrac{\partial^2 \boldsymbol{H}}{\partial t^2}, \tag{3}$$

where the speed of electromagnetic waves is $c = \frac{1}{\sqrt{\epsilon_o \mu_o}}$. All electromagnetic radiation travels, in a vacuum, at the speed $c \approx 2.99792458 \times 10^8 \pm 1.1$ m/s. In any another medium, for electromagnetic waves, the propagation speed is $v = \frac{1}{\sqrt{\epsilon \mu}}$, where ϵ and μ are the electric permittivity and magnetic permeability of that medium, respectively.[3]

2.4 Plane harmonic wave fronts

Now consider the special case of plane harmonic waves, for example of the form

$$\boldsymbol{E} = \boldsymbol{E}_o cos(\boldsymbol{k} \cdot \boldsymbol{x} - \omega t) \qquad \text{and}$$
$$\boldsymbol{H} = \boldsymbol{H}_o cos(\boldsymbol{k} \cdot \boldsymbol{x} - \omega t), \tag{4}$$

where $\boldsymbol{x}$ is an initial position vector to the wave front, where $\boldsymbol{k}$ is the direction of propagation. We refer to the phase as $\phi = \boldsymbol{k} \cdot \boldsymbol{x} - \omega t$, and $\omega = \frac{2\pi}{\tau}$ as the angular frequency, where τ is the period. For plane waves, the wave front is a plane on which ϕ is constant, which is orthogonal to the direction of propagation, characterized by $\boldsymbol{k}$. In the case of harmonic waves, we have

$$\boldsymbol{k} \times \boldsymbol{E} = \mu_o \omega \boldsymbol{H} \qquad \text{and} \qquad \boldsymbol{k} \times \boldsymbol{H} = -\epsilon_o \omega \boldsymbol{E}, \tag{5}$$

and $\boldsymbol{k} \cdot \boldsymbol{E} = 0$ and $\boldsymbol{k} \cdot \boldsymbol{H} = 0$. The three vectors, $\boldsymbol{k}$, $\boldsymbol{E}$ and $\boldsymbol{H}$ constitute a mutually orthogonal triad.[4] The direction of wave propagation is given by $\frac{\boldsymbol{E} \times \boldsymbol{H}}{||\boldsymbol{E} \times \boldsymbol{H}||}$. Electromagnetic waves traveling through space carry electromagnetic power which flows in the direction of wave propagation. The power per unit area flowing perpendicularly into a surface in free space is given by the Poynting vector $\boldsymbol{S} = \boldsymbol{E} \times \boldsymbol{H}$.

[3] The free space electric permittivity is $\epsilon_o = \frac{1}{c^2 \mu_o} = 8.8542 \times 10^{-12}$ C N^{-1} m^{-1} and the free space magnetic permeability is $\mu_o = 4\pi \times 10^{-7}$ Wb A^{-1} m^{-1} $= 1.2566 \times 10^{-6}$ Wb A^{-1} m^{-1}.

[4] By combining the relations in Eq. 5 one obtains $||\boldsymbol{k}|| = \frac{\omega}{c}$.

2.5 Natural (random) electromagnetic power propagation

Since at high-frequencies $\boldsymbol{E}$, $\boldsymbol{H}$ and $\boldsymbol{S}$ oscillate rapidly, it is impractical to measure instantaneous values of $\boldsymbol{S}$ directly. Consider the harmonic representations in Eq. 4 which leads to $\boldsymbol{S} = \boldsymbol{E}_o \times \boldsymbol{H}_o cos^2(\boldsymbol{k} \cdot \boldsymbol{x} - \omega t)$, and consequently the average value over a longer time interval ($\mathcal{T}$) than the time scale of rapid random oscillation,

$$\langle \boldsymbol{S} \rangle_{\mathcal{T}} = \boldsymbol{E}_o \times \boldsymbol{H}_o \langle cos^2(\boldsymbol{k} \cdot \boldsymbol{x} - \omega t) \rangle_{\mathcal{T}} = \tfrac{1}{2} \boldsymbol{E}_o \times \boldsymbol{H}_o, \tag{6}$$

leading to the definition of the *irradiance*

$$I \stackrel{\text{def}}{=} \langle ||\boldsymbol{S}|| \rangle_{\mathcal{T}} = \tfrac{1}{2} ||\boldsymbol{E}_o \times \boldsymbol{H}_o|| = \tfrac{1}{2} \sqrt{\tfrac{\epsilon_o}{\mu_o}} ||\boldsymbol{E}_o||^2. \tag{7}$$

Thus, the power flow is proportional to the square of the amplitude of the electric field.

2.6 Reflection and absorption of power-Fresnel relations

We consider a plane harmonic wave incident upon a plane boundary separating two different materials, specifically vacuum and surface, which produces a reflected wave and an absorbed (refracted) wave (Fig. 2). Two cases for the electric field vector are considered:

(1) Electric field vectors that are parallel (||) to the plane of incidence and
(2) Electric field vectors that are perpendicular ($\perp$) to the plane of incidence.

In either case, the tangential components of the electric and magnetic fields are required to be continuous across the interface. Consider case (1). We have the following general vectorial representations

$$\boldsymbol{E}_{||} = E_{||} cos(\boldsymbol{k} \cdot \boldsymbol{x} - \omega t)\, \boldsymbol{e}_1 \qquad \text{and}$$
$$\boldsymbol{H}_{||} = H_{||} cos(\boldsymbol{k} \cdot \boldsymbol{x} - \omega t)\, \boldsymbol{e}_2, \tag{8}$$

where $\boldsymbol{e}_1$ and $\boldsymbol{e}_2$ are orthogonal to the propagation direction $\boldsymbol{k}$. By employing the law of refraction ($n_i sin\theta_i = n_a sin\theta_a$) we obtain the following conditions relating the incident, reflected and absorbed components of the electric field quantities

$$E_{||i} cos\theta_i - E_{||r} cos\theta_r = E_{||a} cos\theta_a \qquad \text{and}$$
$$H_{\perp i} + H_{\perp r} = H_{\perp a}. \tag{9}$$

Since, for plane harmonic waves, the magnetic and electric field amplitudes are related by $H = \frac{E}{v\mu}$, we have

$$E_{||i} + E_{||r} = \frac{\mu_i}{\mu_a}\frac{v_i}{v_a}E_{||a} = \frac{\mu_i}{\mu_a}\frac{n_a}{n_i}E_{||a} \stackrel{\text{def}}{=} \frac{\hat{n}}{\hat{\mu}}E_{||a}, \tag{10}$$

where $\hat{\mu} \stackrel{\text{def}}{=} \frac{\mu_a}{\mu_i}$, $\hat{n} \stackrel{\text{def}}{=} \frac{n_a}{n_i}$ and where v_i, v_r and v_a are the values of the velocity in the incident, reflected and absorbed directions.[5] By again employing the law of refraction, we obtain the Fresnel reflection and transmission/absorption coefficients, generalized for the case of unequal magnetic permeabilities

$$\begin{aligned} r_{||} &= \frac{E_{||r}}{E_{||i}} = \frac{\frac{\hat{n}}{\hat{\mu}}cos\theta_i - cos\theta_a}{\frac{\hat{n}}{\hat{\mu}}cos\theta_i + cos\theta_a} \quad \text{and} \\ a_{||} &= \frac{E_{||a}}{E_{||i}} = \frac{2cos\theta_i}{cos\theta_a + \frac{\hat{n}}{\hat{\mu}}cos\theta_i}. \end{aligned} \tag{11}$$

Following the same procedure for case (2), where the components of $\boldsymbol{E}$ are perpendicular to the plane of incidence, we have

$$\begin{aligned} r_{\perp} &= \frac{E_{\perp r}}{E_{\perp i}} = \frac{cos\theta_i - \frac{\hat{n}}{\hat{\mu}}cos\theta_a}{cos\theta_i + \frac{\hat{n}}{\hat{\mu}}cos\theta_a} \quad \text{and} \\ a_{\perp} &= \frac{E_{\perp a}}{E_{\perp i}} = \frac{2cos\theta_i}{cos\theta_i + \frac{\hat{n}}{\hat{\mu}}cos\theta_a}. \end{aligned} \tag{12}$$

Our primary interest is in the reflections. We define the reflectances as

$$\mathcal{IR}_{||} \stackrel{\text{def}}{=} r_{||}^2 \qquad \text{and} \qquad \mathcal{IR}_{\perp} \stackrel{\text{def}}{=} r_{\perp}^2. \tag{13}$$

Particularly convenient forms for the reflections are

$$\begin{aligned} r_{||} &= \frac{\frac{\hat{n}^2}{\hat{\mu}}cos\theta_i - (\hat{n}^2 - sin^2\theta_i)^{\frac{1}{2}}}{\frac{\hat{n}^2}{\hat{\mu}}cos\theta_i + (\hat{n}^2 - sin^2\theta_i)^{\frac{1}{2}}} \quad \text{and} \\ r_{\perp} &= \frac{cos\theta_i - \frac{1}{\hat{\mu}}(\hat{n}^2 - sin^2\theta_i)^{\frac{1}{2}}}{cos\theta_i + \frac{1}{\hat{\mu}}(\hat{n}^2 - sin^2\theta_i)^{\frac{1}{2}}}. \end{aligned} \tag{14}$$

Thus, the total power reflected can be characterized by

$$\mathcal{IR} \stackrel{\text{def}}{=} \left(\frac{E_r}{E_i}\right)^2 = \frac{E_{\perp r}^2 + E_{||r}^2}{E_i^2} = \frac{I_{||r} + I_{\perp r}}{I_i}. \tag{15}$$

If the resultant plane of oscillation of the (polarized) wave makes an angle of γ_i with the plane of incidence, then

$$E_{||i} = E_i cos\gamma_i \qquad \text{and} \qquad E_{\perp i} = E_i sin\gamma_i, \tag{16}$$

and it follows from the previous definition of I that

$$I_{||i} = I_i cos^2\gamma_i \qquad \text{and} \qquad I_{\perp i} = I_i sin^2\gamma_i. \tag{17}$$

Substituting these expressions back into the equations for the reflectances yields

$$\mathcal{IR} = \frac{I_{||r}}{I_i}cos^2\gamma_i + \frac{I_{\perp r}}{I_i}sin^2\gamma_i = \mathcal{IR}_{||}cos^2\gamma_i + \mathcal{IR}_{\perp}sin^2\gamma_i. \tag{18}$$

For natural or unpolarized electromagnetic radiation, the angle γ_i varies rapidly in a random manner, as does the field amplitude. Thus, since

$$\langle cos^2\gamma_i(t)\rangle_{\mathcal{T}} = \tfrac{1}{2} \qquad \text{and} \qquad \langle sin^2\gamma_i(t)\rangle_{\mathcal{T}} = \tfrac{1}{2}, \tag{19}$$

and therefore for natural electromagnetic radiation

$$I_{||i} = \tfrac{I_i}{2} \qquad \text{and} \qquad I_{\perp i} = \tfrac{I_i}{2}. \tag{20}$$

and therefore

$$r_{||}^2 = \left(\frac{E_{||r}^2}{E_{||i}^2}\right)^2 = \frac{I_{||r}}{I_{||i}} \qquad \text{and} \qquad r_{\perp}^2 = \left(\frac{E_{\perp r}^2}{E_{\perp i}^2}\right)^2 = \frac{I_{\perp r}}{I_{\perp i}}. \tag{21}$$

Thus, the total reflectance becomes

$$\mathcal{IR} = \frac{1}{2}(\mathcal{IR}_{||} + \mathcal{IR}_{\perp}) = \frac{1}{2}(r_{||}^2 + r_{\perp}^2), \tag{22}$$

where $0 \le \mathcal{IR} \le 1$. For the cases where $sin\theta_a = \frac{sin\theta_i}{\hat{n}} > 1$, one may rewrite reflection relations as

$$\begin{aligned} r_{||} &= \frac{\frac{\hat{n}^2}{\hat{\mu}}cos\theta_i - j(sin^2\theta_i - \hat{n}^2)^{\frac{1}{2}}}{\frac{\hat{n}^2}{\hat{\mu}}cos\theta_i + j(sin^2\theta_i - \hat{n}^2)^{\frac{1}{2}}} \quad \text{and} \\ r_{\perp} &= \frac{cos\theta_i - \frac{1}{\hat{\mu}}j(sin^2\theta_i - \hat{n}^2)^{\frac{1}{2}}}{cos\theta_i + \frac{1}{\hat{\mu}}j(sin^2\theta_i - \hat{n}^2)^{\frac{1}{2}}} \end{aligned} \tag{23}$$

where, $j = \sqrt{-1}$, and in this complex case[6]

$$\mathcal{IR}_{||} \stackrel{\text{def}}{=} r_{||}\bar{r}_{||} = 1, \qquad \text{and} \qquad \mathcal{IR}_{\perp} \stackrel{\text{def}}{=} r_{\perp}\bar{r}_{\perp} = 1, \tag{24}$$

where $\bar{r}_{||}$ and $\bar{r}_{\perp}$ are complex conjugates. Thus, for angles above the critical angle θ_i^*, all of the power is reflected. Notice that as $\hat{n} \to 1$ we have complete absorption, while as $\hat{n} \to \infty$ we have complete reflection. The amount of absorbed irradiance by the surface is $I_a = (1 - \mathcal{IR})I_i$.

[5] Throughout the analysis we assume that $\hat{n} \ge 1$.

[6] The limiting case $\frac{sin\theta_i^*}{\hat{n}} = 1$, is the critical angle (θ_i^*) case.

2.7 Reflectivity

To observe the dependency of $\mathcal{IR}$ on $\hat{n}$ and θ_i we can explicitly write

$$\mathcal{IR} = \frac{1}{2}\left(\left(\frac{\frac{\hat{n}^2}{\hat{\mu}}cos\theta_i - (\hat{n}^2 - sin^2\theta_i)^{\frac{1}{2}}}{\frac{\hat{n}^2}{\hat{\mu}}cos\theta_i + (\hat{n}^2 - sin^2\theta_i)^{\frac{1}{2}}}\right)^2 + \left(\frac{cos\theta_i - \frac{1}{\hat{\mu}}(\hat{n}^2 - sin^2\theta_i)^{\frac{1}{2}}}{cos\theta_i + \frac{1}{\hat{\mu}}(\hat{n}^2 - sin^2\theta_i)^{\frac{1}{2}}}\right)^2\right). \tag{25}$$

We observe:

- As $\hat{n} \to \infty$, $\mathcal{IR} \to 1$, no matter what the angle of incidence's value. We note that as $\hat{n} \to 1$, provided that $\hat{\mu} = 1$, $\mathcal{IR} \to 0$, i.e. all incident power is absorbed (it is transparent).
- With increasing $\hat{n}$, the angle for minimum reflectance grows larger. As mentioned previously, for the remainder of the work, we shall take $\hat{\mu} = 1$ ($\mu_o = \mu_i = \mu_a$), thus

$$\hat{n} = \frac{n_a}{n_i} = \sqrt{\frac{\epsilon_a \mu_a}{\epsilon_i \mu_i}} \Rightarrow \epsilon_a \mu_a = (\hat{n})^2 \epsilon_i \mu_i \Rightarrow \epsilon_a = (\hat{n})^2 \epsilon_i. \tag{26}$$

- The previous assumption yields

$$\mathcal{IR} = \frac{I_r}{I_i} = \frac{1}{2}\left(\left(\frac{\hat{n}^2 cos\theta_i - (\hat{n}^2 - sin^2\theta_i)^{\frac{1}{2}}}{\hat{n}^2 cos\theta_i + (\hat{n}^2 - sin^2\theta_i)^{\frac{1}{2}}}\right)^2 + \left(\frac{cos\theta_i - (\hat{n}^2 - sin^2\theta_i)^{\frac{1}{2}}}{cos\theta_i + (\hat{n}^2 - sin^2\theta_i)^{\frac{1}{2}}}\right)^2\right). \tag{27}$$

Remark 1 Recall that $\bar{I}$ is the power per unit area, and that we obtain the power associated with an entire pulse/beam by multiplying the irradiance by the cross-sectional area of an initially coherent beam, $\bar{I}A^b$, where A^b is the cross-sectional area of the beam (comprising all of the rays). The power in a ray in the pulse/beam is then given by $I = \bar{I}A^r = \bar{I}A^b/N_r$, where N_r is the number of rays in the beam (Fig. 2) and A^r can be considered the area associated with a ray. The reflection relation, Eq. 25, can then be used to compute changes in the magnitude of the reflected rays (and the amount absorbed), with directional changes given by the laws of reflection. We refer the reader to Gross [26] and Zohdi [28–34] for details.

Remark 2 We have the following additional observations:

- The angle between the point of contact of a ray (Fig. 2) and the outward normal to the surface at that point is the angle of incidence, θ_i. The classical reflection law states that the angle at which a ray is reflected is the same as the angle of incidence and that the incoming (incident, θ_i) and outgoing (reflected, θ_r) ray lays in the same plane, and $\theta_i = \theta_r$.
- The classical refraction law states that, if the ray passes from one medium into a second one (with a different index of refraction) and, if the index of refraction of the second medium is less than that of the first, the angle the ray makes with the normal to the interface is always less than the angle of incidence, where $\hat{n} \stackrel{\text{def}}{=} \frac{v_i}{v_a} = \sqrt{\frac{\epsilon_a \mu_a}{\epsilon_i \mu_i}} = \frac{sin\theta_i}{sin\theta_a}$, θ_a being the angle of the absorbed ray (Fig. 2).

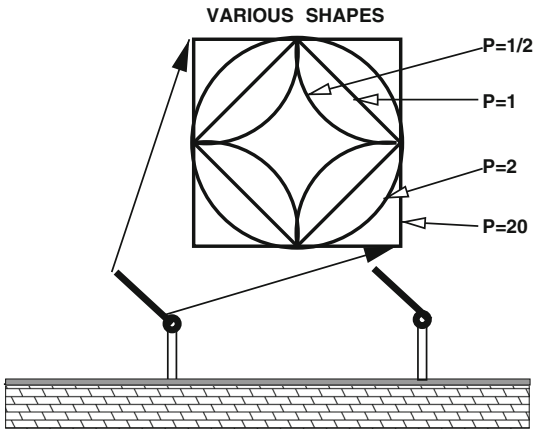

Fig. 3 Possible panel shapes (cross-sections) generated from a generalized 3D-ellipsoidal equation (Eq. 28)

3 Power propagation tracking algorithm

From this point forth, we assume that the ambient medium behaves as a vacuum. Accordingly, there are no energetic losses as the rays move through the surrounding medium. Starting at $t = 0$ and ending at $t = T$, the simple overall algorithm to track rays is as follows, at each time increment:

1. Check for intersections of rays with surfaces (hence a reflection), and compute the ray magnitudes and orientation if there are reflections (for all rays that are experiencing a reflection, I_j^{ref}, $j = 1, 2, \ldots, Rays$),
2. Increment all ray positions ($\boldsymbol{r}_j(t + \Delta t) = \boldsymbol{r}_j(t) + \Delta t \boldsymbol{v}_j(t)$, $j = 1, 2, \ldots, Rays$),
3. Increment time forward ($t = t + \Delta t$) and repeat the process for the next time interval.

In order to capture all of the ray reflections that occur:

- The time step size Δt is dictated by the offset height of the source. A somewhat ad-hoc approach is to scale the time step size by the speed of ray propagation according to $\Delta t = \xi \frac{\mathcal{H}}{||\boldsymbol{v}||}$, where $\mathcal{H}$ is the height of the source and

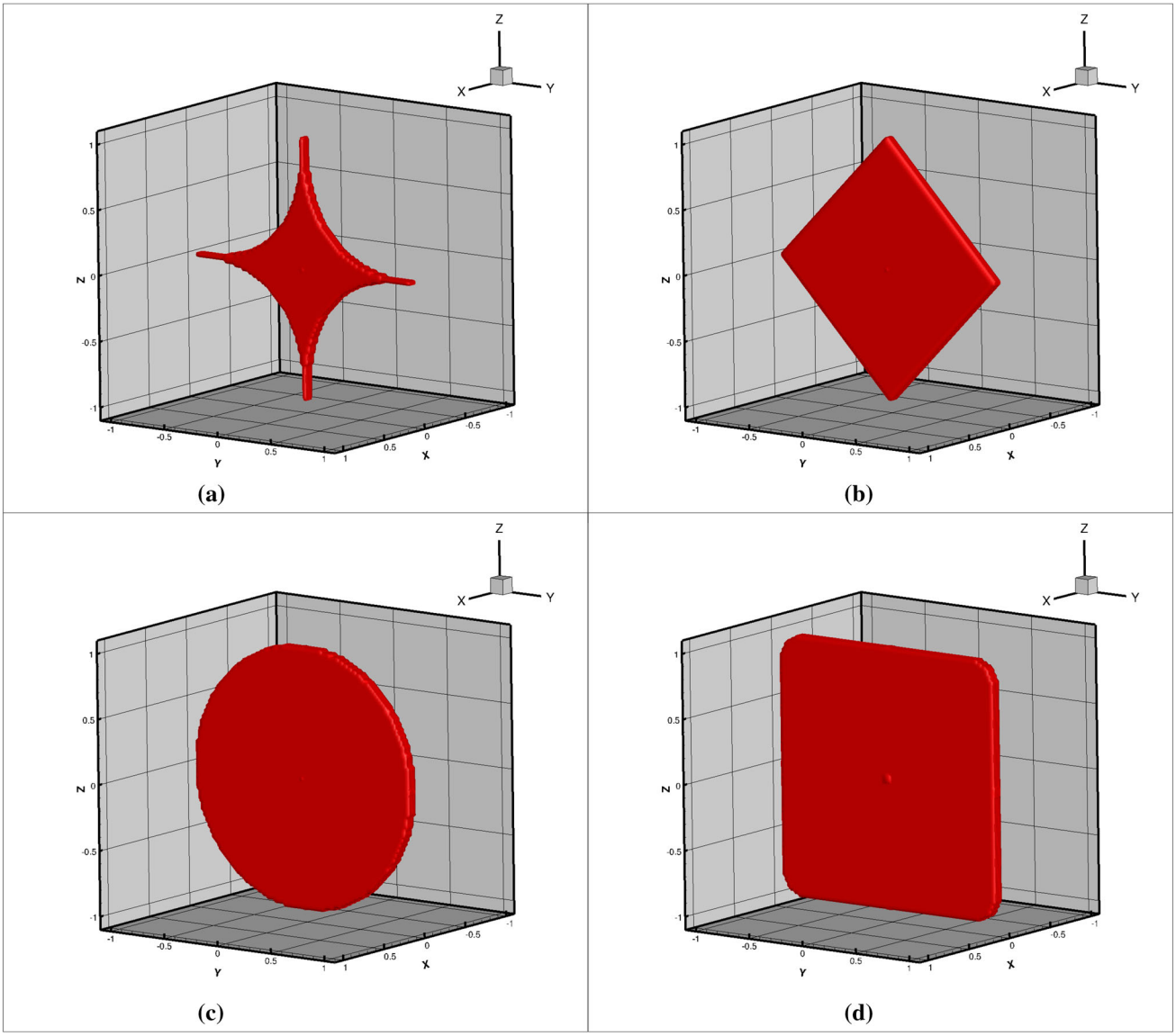

Fig. 4 Examples for (a) $(p_1, p_2, p_3) = (10, 1/2, 1/2)$ and $(R_1, R_2, R_3) = (1/20, 1, 1)$, (b) $(p_1, p_2, p_3) = (10, 1, 1)$ and $(R_1, R_2, R_3) = (1/20, 1, 1)$, (c) $(p_1, p_2, p_3) = (10, 2, 2)$ and $(R_1, R_2, R_3) = (1/20, 1, 1)$ and (d) $(p_1, p_2, p_3) = (10, 10, 10)$ and $(R_1, R_2, R_3) = (1/20, 1, 1)$ for a generalized 3D-ellipsoidal equation (Eq. 28)

$0.0001 \leq \xi \leq 0.01$. Typically, the results are insensitive to ξ that are smaller than this range.

- Although outside the scope of this work, one can also use this algorithm to compute the thermal response by combining it with heat transfer equations via staggering schemes (Zohdi [28,31]).

4 Panel surface model

The discrete-ray approach is flexible enough to simulate a wide variety of systems. This also aligns with advances in manufacturing, 3D-printing, etc. that allow for many possible shapes to be fabricated. For the solar panels, we consider a topology described by the normalized equation for a surface, $F(x_1, x_2, x_3) = 1$ (Figs. 3, 4). Specifically, a generalized 3D-ellipsoidal equation (Eq. 28) is used where for exponent values of (p_1, p_2, p_3) equal to two, $(2, 2, 2)$, we generate a familiar 3D-ellipsoidal surface, for values less than one we generate involute (nonconvex shapes and corresponding surfaces), and for exponent values of (p_1, p_2, p_3) greater than two, we generate a box-like shapes (Figs. 3, 4). To generate a panel, a generalized 3D-ellipsoidal equation is used

$$F(x_1, x_2, x_3) = \|\frac{x_1 - x_{1o}}{R_1}\|^{p_1} + \|\frac{x_2 - x_{2o}}{R_2}\|^{p_2} + \|\frac{x_3 - x_{3o}}{R_3}\|^{p_3} = 1 \tag{28}$$

where (x_{1o}, x_{2o}, x_{3o}) are the coordinates panel center and (R_1, R_2, R_3) are the generalized radii and (p_1, p_2, p_3) are exponents of the generalized 3D-ellipsoid, which ultimately will be design variables in the Machine-Learning Algorithm discussed later. Intersections of a ray with a surface are achieved by checking the intersection with the surface of the 3D-ellipsoidal equation (Eq. 28) The outward surface normals, $\boldsymbol{n}$, needed during the scattering calculations, are easy to characterize by writing

$$\boldsymbol{n} = \frac{\nabla F}{||\nabla F||}, \tag{29}$$

where the components of the gradient are

$$\nabla F = \frac{\partial F}{\partial x_1}\boldsymbol{e}_1 + \frac{\partial F}{\partial x_2}\boldsymbol{e}_2 + \frac{\partial F}{\partial x_3}\boldsymbol{e}_3. \tag{30}$$

5 Numerical/quantitative examples

We have the following examples:

- The initial velocity vector for all initially collimated (parallel) rays comprising the beam was $\boldsymbol{v} = (c, 0, 0)$, where $c = 3 \times 10^8$ m/s is the speed of light in a vacuum. Initially, the rays are randomly placed in a square that is 1.5 times the size of the target area, all pointing in parallel in the same direction connecting the center of the target area and the square containing the rays.
- We used a parametrized test surface given by Eq. 28, $(p_1, p_2, p_3) = (10, 10, 10)$ and $(R_1, R_2, R_3) = (1/20, 1, 1)$ for a generalized 3D-ellipsoidal equation (Eq. 28). This corresponds to square panels. The panels were also rotated (and fixed) 45° about the x_2/y axis.
- The number of rays in the beam were steadily increased from $N_r = 100, 200, etc$, until the results were insensitive to further refinements-*at approximately* $2000 \leq N_r \leq 2500$ *parallel rays in rectangular cross-sectional plane of the beam.* The rays were randomly placed within the beam (Fig. 2), to correspond to unpolarized incoming power.
- To illustrate the propagation of light for one incoming source scenario, the rays come from the left at an angle and "plow" through the farm. There were 16 panels in the simulation, equally spaced in a 4×4 grid and all oriented in the same direction. Only the surfaces that have been previously contacted by the rays (with corresponding power absorbed) are shown, which in this case were 8 panels. This allows for easy viewing of where the power is going. The length and color of the directed rays indicate the power content (Watts), where orange is the raw, unreflected power from the source (for example, the sun), while the blue arrows (as well as other color between orange and blue) indicate smaller power content, due to multiple reflections. The vector directions indicate the propagation direction of power flow. The length and color of the directed rays indicate the power content (Watts), where orange is the raw, unreflected power from the source (for example, the sun) which the blue arrows (as well as other color between orange and blue) indicate smaller power content, due to multiple reflections. The vector directions indicate the propagation direction of power flow.
- Figure 5 illustrates the results for five different incoming light scenarios: Case 1: parallel rays emanating from $(-1.0, 0.0, 0.65)$, Case 2: parallel rays emanating from $(-0.5, 0.0, 0.65)$, Case 3: parallel rays emanating from $(0.0, 0.0, 0.65)$, Case 4: parallel rays emanating from $(0.5, 0.0, 0.65)$ and Case 5: parallel rays emanating from $(1.0, 0.0, 0.65)$. Initially, the rays are randomly placed in a square that is 1.5 times the size of the target area, all pointing in parallel in the same direction connecting the center of the target area and the square containing the rays.
- This Digital-Twin facilitates quick quantification of the absorption efficacy across the topology of the structure (color coding the efficacy relative to the incoming irradiation) and parametric studies for the changes in absorption as a function of changes in surface geometry. *The simulations take a fraction of a second on a laptop.* This type of approach makes it quite suitable for use in conjunction with mobile APV systems and provides a simpler alternative to a direct, computationally intensive, discretization of a continuum description using Maxwell's equations with a Finite Element or Finite Difference method.

Remark 3 If desired, this approach also allows an analyst to explore nonuniform beam profiles, for example exponential central irradiance decay: $I(d) = I(d = 0)e^{-ad}$, where d is the distance from the center of the initial beam, where in the case of $a = 0$, one recaptures a flat beam, $I(d) = I(d = 0)$.[7]

[7] Note that algorithmically, we can the set total initial irradiance via $\sum_{i=1}^{N_r} I_i^{inc}(t = 0)\mathcal{A}_r = P$ Watts. To achieve this distribution, one would first place rays randomly in the plane, and then scale the individual I^{inc} by e^{-ad} and the normalized the average so that the total was P Watts.

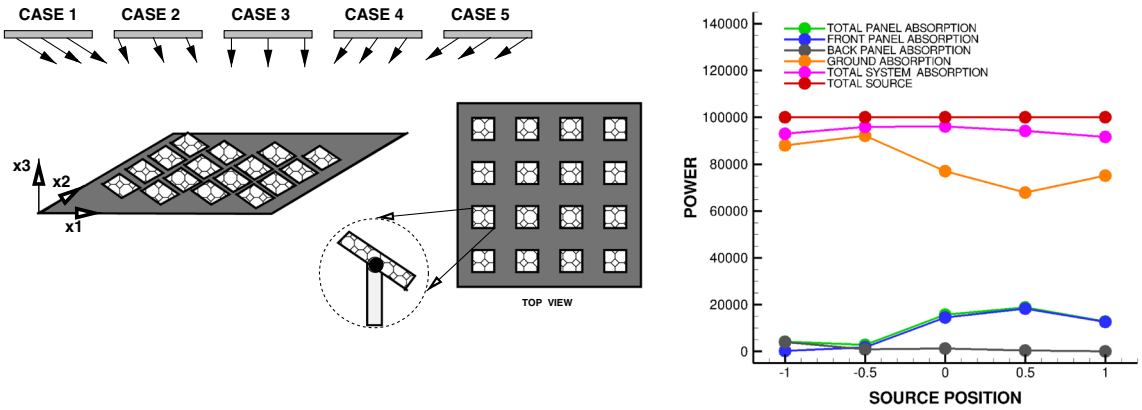

Fig. 5 The results of performance for 5 different incoming solar scenarios. Case 1: parallel rays emanating from $(-1.0, 0.0, 0.65)$, Case 2: parallel rays emanating from $(-0.5, 0.0, 0.65)$, Case 3: parallel rays emanating from $(0.0, 0.0, 0.65)$, Case 4: parallel rays emanating from $(0.5, 0.0, 0.65)$ and Case 5: parallel rays emanating from $(1.0, 0.0, 0.65)$. Initially, the rays are randomly placed in a square that is 1.5 times the size of the target area, all pointing in parallel in the same direction connecting the center of the target area and the square containing the rays

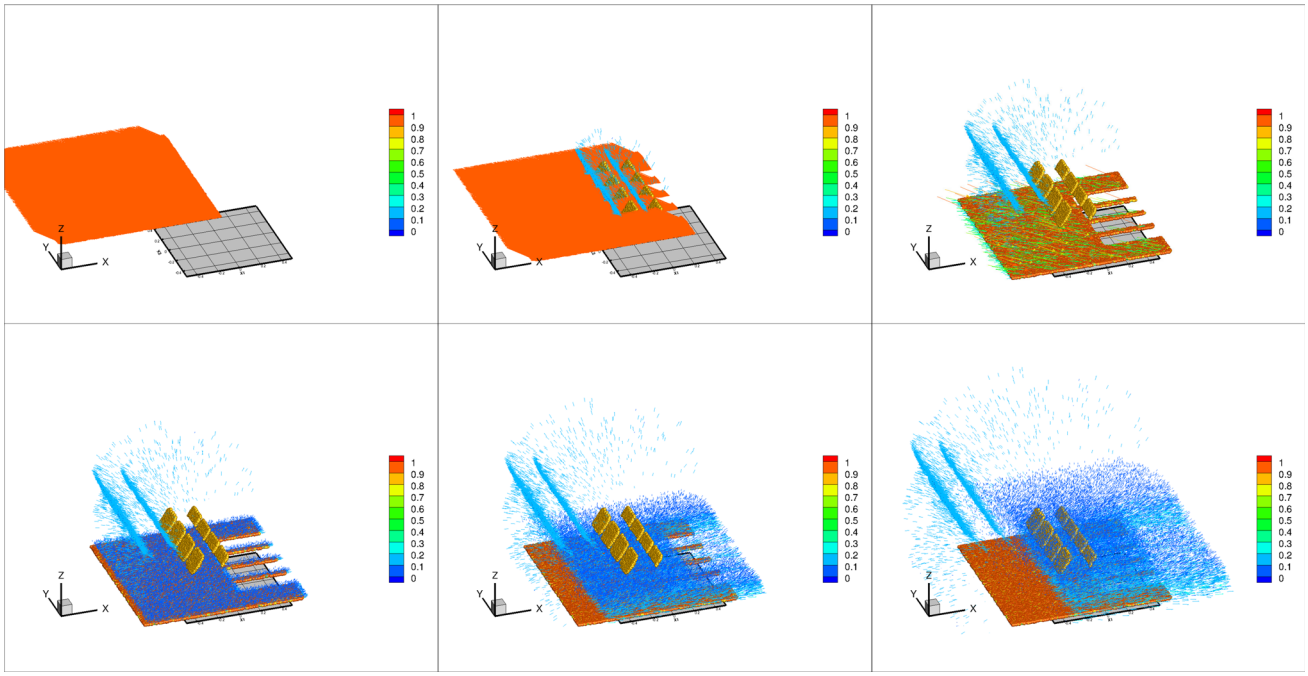

Fig. 6 Frames associated with one solar farm configuration and one incoming source scenario. The rays come from the left at an angle and "plow" through the farm. There were 16 panels in the simulation, equally spaced in a 4×4 grid and all oriented in the same direction. Only the surfaces that have been contacted by the rays are exposed, which in this case were 8 panels. The length and color of the directed rays indicate the power content (Watts), where orange is the raw, unreflected power from the source (for example, the sun), while the blue arrows (as well as other color between orange and blue) indicate smaller power content, due to multiple reflections. The vector directions indicate the propagation direction of power flow

6 Genomic machine-learning framework

The rapid rate at which these simulations can be completed enables the ability to explore inverse problems seeking to determine what parameter combinations can deliver a desired result. Following Zohdi [41–44] , we formulate the objective as a cost function minimization problem that seeks system parameters that match a desired response by minimizing a cost/error function $\Pi(\mathbf{\Lambda})$. Specifically, we use

$$\Pi = w_1 \alpha + w_2 \gamma, \tag{31}$$

where the panel loss ratio is $\alpha = \frac{Panel\ Losses}{Total\ Input}$, which signifies the power not captured by the panels, and γ represents a range of ground absorption given by

- $If\ G\ \geq G^{+}\ then\ \gamma = |G - G^{+}|$,
- $If\ G\ \leq G^{-}\ then\ \gamma = |G - G^{-}|$ and
- $If\ G^{-} < G\ < G^{+}\ then\ \gamma = 0$,

where the ground absorption ratio is $G = \frac{Ground\ Absorption}{Total\ Input}$, G^{+} is the upper bound for the fraction of solar power absorbed by the ground and G^{-} is the lower bound for the fraction of solar power absorbed by the ground. We systematically minimize Π, by varying the design parameters: $\mathbf{\Lambda}^{i} \overset{\text{def}}{=} \{\Lambda_1^i, \Lambda_2^i, \Lambda_3^i, \ldots, \Lambda_N^i\} \overset{\text{def}}{=} \{panel\ size,\ spacing,\ angles\ \ldots\}$. The system parameter search is conducted within the constrained ranges of $\Lambda_1^{(-)} \leq \Lambda_1 \leq \Lambda_1^{(+)}$, $\Lambda_2^{(-)} \leq \Lambda_2 \leq \Lambda_2^{(+)}$ and $\Lambda_3^{(-)} \leq \Lambda_3 \leq \Lambda_3^{(+)}$, etc. These upper and lower limits would, in general, be dictated by what is physically feasible. The system parameters to vary and optimize the following (12) parameters: (1) Panel inclination (3 angles), (2) Refractive index of panels (front and back, 1 parameter), (3) Dimensions of panels (3 parameters), (4) Shape of panels (3 parameters), (5) Ground refractive index (1 parameter) and (6) Panel placement above ground (1 parameter).

6.1 System parameter search/machine-learning algorithm (MLA)

Cost functions such as Π are nonconvex in design parameter space and often nonsmooth. Their minimization is usually difficult with direct application of gradient methods. This motivates nonderivative search methods, for example those found in Machine-Learning Algorithms (MLA's). One of the most basic subsets of MLA's are so-called Genetic Algorithms (GA's). For a review of GA's, see the pioneering work of John Holland ([35,36]), as well as Goldberg [37], Davis [38], Onwubiko [39] and Goldberg and Deb [40]. A description of the algorithm will be described next (Zohdi [41–44]).

6.2 Algorithmic structure

The MLA/GA approach is extremely well-suited for nonconvex, nonsmooth, multicomponent, multistage systems and, broadly speaking, involves the following essential concepts (Fig. 7):

1. *Population generation* Generate a parameter population of genetic strings: $\mathbf{\Lambda}^{i}$
2. *Performance evaluation* Compute performance of each genetic string: $\Pi(\mathbf{\Lambda}^{i})$
3. *Rank strings* Rank them $\mathbf{\Lambda}^{i}$, $i = 1, \ldots, S$
4. *Mating process* Mate pairs/produce offspring
5. *Gene elimination* Eliminate poorly performing genetic strings
6. *Population regeneration* Repeat process with updated gene pool and new *random* genetic strings
7. *Solution post-processing* Employ gradient-based methods afterwards in local "valleys"-*if smooth enough*

6.3 Specifics

Following Zohdi [41–44], the algorithm is as follows:

- *STEP 1:* Randomly generate a population of S starting genetic strings, $\mathbf{\Lambda}^{i}$, $(i = 1, 2, 3, \ldots, S)$:

$$\mathbf{\Lambda}^{i} \overset{\text{def}}{=} \left\{ \begin{array}{c} \Lambda_1^i \\ \Lambda_2^i \\ \Lambda_3^i \\ \ldots \\ \Lambda_N^i \end{array} \right\} \tag{32}$$

- *STEP 2:* Compute fitness of each string $\Pi(\mathbf{\Lambda}^{i})$, (i=1, …, S)
- *STEP 3:* Rank genetic strings: $\mathbf{\Lambda}^{i}$, (i=1, …, S)
- *STEP 4:* Mate nearest pairs and produce two offspring, (i=1, …, S):

$$\boldsymbol{\lambda}^{i} \overset{\text{def}}{=} \boldsymbol{\Phi} \circ \mathbf{\Lambda}^{i} + (\mathbf{1} - \boldsymbol{\Phi}) \circ \mathbf{\Lambda}^{\mathbf{i+1}} \overset{\text{def}}{=} \left\{ \begin{array}{c} \phi_1 \Lambda_1^i \\ \phi_2 \Lambda_2^i \\ \phi_3 \Lambda_3^i \\ \ldots \\ \phi_N \Lambda_N^i \end{array} \right\} + \left\{ \begin{array}{c} (1-\phi_1)\Lambda_1^{i+1} \\ (1-\phi_2)\Lambda_2^{i+1} \\ (1-\phi_3)\Lambda_3^{i+1} \\ \ldots \\ (1-\phi_N)\Lambda_N^{i+1} \end{array} \right\} \tag{33}$$

and

$$\boldsymbol{\lambda}^{i+1} \overset{\text{def}}{=} \boldsymbol{\Psi} \circ \mathbf{\Lambda}^{i} + (\mathbf{1} - \boldsymbol{\Psi}) \circ \mathbf{\Lambda}^{\mathbf{i+1}} \overset{\text{def}}{=} \left\{ \begin{array}{c} \psi_1 \Lambda_1^i \\ \psi_2 \Lambda_2^i \\ \psi_3 \Lambda_3^i \\ \ldots \\ \psi_N \Lambda_N^i \end{array} \right\} + \left\{ \begin{array}{c} (1-\psi_1)\Lambda_1^{i+1} \\ (1-\psi_2)\Lambda_2^{i+1} \\ (1-\psi_3)\Lambda_3^{i+1} \\ \ldots \\ (1-\psi_N)\Lambda_N^{i+1} \end{array} \right\} \tag{34}$$

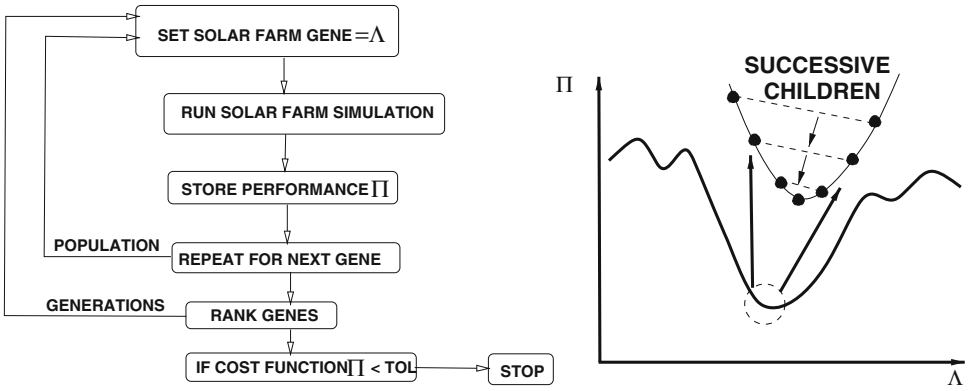

Fig. 7 Left, an overall flow chart and right, the basic action of a MLA/GA Machine-Learning Algorithm/Genetic Algorithm (Zohdi [41–44])

where for this operation, the ϕ_i and ψ_i are random numbers, such that $0 \leq \phi_i \leq 1$, $0 \leq \psi_i \leq 1$, which are different for each component of each genetic string

- *STEP 5:* Eliminate the bottom M strings and keep top K parents and their K offspring (K offspring+K parents+M=S)
- *STEP 6:* Repeat STEPS 1-5 with top gene pool (K offspring and K parents), plus M new, randomly generated, strings
- *IMPORTANT OPTIONS:* One can rescale and restart search around best performing parameter set every few generations. Typically, one will use a GA first in order to isolate multiple local minima, and then use a gradient-based algorithm in these locally convex regions or reset the GA to concentrate its search over these more constrained regions.

Remark 4 If one selects the mating parameters $\phi's$ and $\gamma's$ to be greater than one and/or less than zero, one can induce "mutations", i.e. characteristics that neither parent possesses. However, this is somewhat redundant with introduction of new random members of the population in the current algorithm. If one does not retain the parents in the algorithm above, it is possible that inferior performing offspring may replace superior parents. Thus, top parents should be kept for the next generation. This guarantees a monotone reduction in the cost function. Furthermore, retained parents do not need to be reevaluated, making the algorithm less computationally less expensive, since these parameter sets do not have to be reevaluated (or ranked) in the next generation. Numerous studies of the author (Zohdi [41–44]) have shown that the advantages of parent retention outweighs inbreeding, for sufficiently large population sizes. Finally, we remark that this algorithm is easily parallelizeable. After application of such a global search algorithm, one can apply a gradient-based method, if the objective function is sufficiently smooth in that region of the parameter space. In other words, if one has located a convex portion of the parameter space with a global genetic search, one can employ gradient-based procedures locally to minimize the objective function further, since they are generally much more efficient for convex optimization of smooth functions. An exhaustive review of these methods can be found in the texts of Luenberger [45] and Gill, Murray and Wright [46].

6.4 Algorithmic settings

In the upcoming example, the design parameters $\mathbf{\Lambda} = \{\Lambda_1, \Lambda_2 \ldots \Lambda_N\}$ are optimized over the search intervals (12 variables): $\mathbf{\Lambda}_i^- \leq \mathbf{\Lambda}_i \leq \mathbf{\Lambda}_i^+$, $i = 1, 2, \ldots, 12$. Specifically (Fig. 8), we varied the following parameters: (a) Panel inclination (3 angles), (b) Refractive index of panels (front and back, 1 parameter), (c) Dimensions of panels (3 parameters), (d) Shape of panels (3 parameters), (e) Ground refractive index (1 parameter) and (f) Panel height above ground (1 parameter). Figure 9 shows the reduction of the cost function for the 12 parameter set. Shown are the best performing gene (design parameter set, in *red*) as a function of successive generations, as well as the average performance of the entire population of the genes (designs, in *green*). We used the following MLA settings:

- Number of design variables: 12,
- Population size per generation: 24,
- Number of parents to keep in each generation: 6,
- Number of children created in each generation: 6,
- Number of completely new genes created in each generation: 12,
- Number of generations for re-adaptation around a new search interval: 10 and
- Number of generations: 1000.

6.5 Parameter search ranges and results

We considered a 16 panel farm, where the panels are equally-spaced in a square pattern. All panels are identical. The

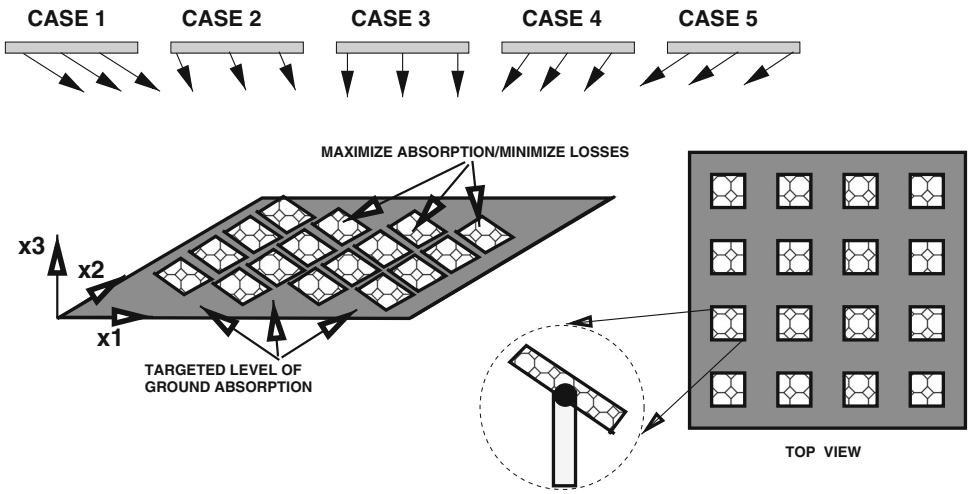

Fig. 8 The system to be optimized: 16 panels, equally spaced. The following parameters were varied: **a** panel inclination (3 angles), **b** refractive index of panels (front and back, 1 parameter), **c** dimensions of panels (3 parameters), **d** shape of panels (3 parameters), **e**) ground refractive index (1 parameter) and **f** panel height above ground (1 parameter)

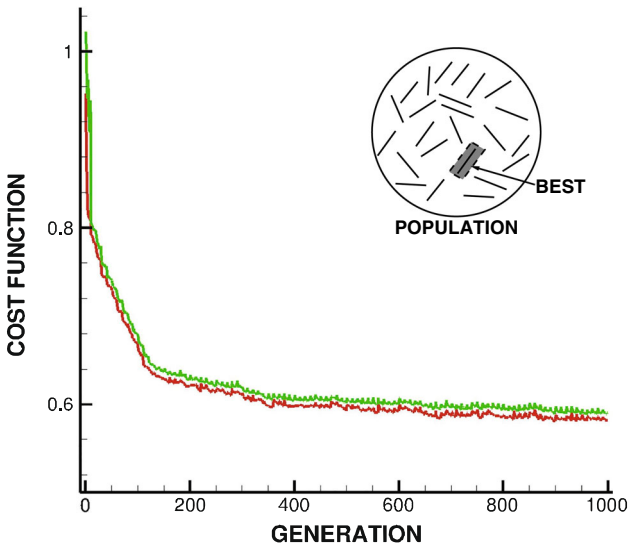

Fig. 9 Optimization of performance of a single fixed solar farm configuration for 5 different incoming light conditions. Shown are the cost function for the best performing gene (*red*) as a function of successive generations, as well as the average cost function of the entire population of genes (*green*). We allowed the MLA/GA to readapt every 10 generations, leading to the (slight) nonmonotone reduction of the cost function. Often, this action is more efficient than allowing the algorithm not to readapt, since it probes around the current optimum for better local alternatives

following search parameter ranges were used (with $w_1 = 1$ and $w_2 = 0.5$):

- Λ_1 = Rotation angle 1 (relative to the x_1-axis):$\Lambda_1^- = -0.5\pi \le \Lambda_1 \le \Lambda_1^+ = 0.5\pi$,
- Λ_2 = Rotation angle 2 (relative to the x_2-axis):$\Lambda_2^- = -0.5\pi \le \Lambda_2 \le \Lambda_2^+ = 0.5\pi$,
- Λ_3 = Rotation angle 3 (relative to the x_3-axis): $\Lambda_3^- = -0.5\pi \le \Lambda_3 \le \Lambda_3^+ = 0.5\pi$,
- Λ_4 = Panel refractive index: $\Lambda_4^- = 1.0 \le \Lambda_4 \le \Lambda_4^+ = 100$,
- Λ_5 = Ground refractive index:$\Lambda_5^- = 1.0 \le \Lambda_5 \le \Lambda_5^+ = 100$,
- Λ_6 = Panel R_1 size:$\Lambda_6^- = 0.005 \le \Lambda_6 \le \Lambda_6^+ = 0.01$,
- Λ_7 = Panel R_2 size:$\Lambda_7^- = 0.0125 \le \Lambda_7 \le \Lambda_7^+ = 0.125$,
- Λ_8 = Panel R_3 size:$\Lambda_8^- = 0.0125 \le \Lambda_8 \le \Lambda_8^+ = 0.125$,
- Λ_9 = Shape Parameter p_1:$\Lambda_9^- = 1 \le \Lambda_9 \le \Lambda_9^+ = 20$,
- Λ_{10} = Shape Parameter p_2:$\Lambda_{10}^- = 1 \le \Lambda_{10} \le \Lambda_{10}^+ = 20$,
- Λ_{11} = Shape Parameter p_3:$\Lambda_{11}^- = 1 \le \Lambda_{11} \le \Lambda_1^+ = 20$,
- Λ_{12} = height h: $\Lambda_{12}^- = 0.25 \le \Lambda_{12} \le \Lambda_{12}^+ = 0.5$.

Figure 9 illustrates the results for the cost function for the best performing gene (*red*) as a function of successive generations, as well as the average performance cost function of the entire population of genes (designs, in *green*), using design weights of $w_1 = 1$ and $w_2 = 0.5$, indicating that minimizing panel losses was twice as important (in this example) as meeting ground absorption targets. We allowed the MLA/GA

Table 1 The system parameters ($\mathbf{\Lambda}_1 - \mathbf{\Lambda}_{12}$) for the best performing design (gene)

w_1	w_2	$\mathbf{\Lambda}_1$	$\mathbf{\Lambda}_2$	$\mathbf{\Lambda}_3$	$\mathbf{\Lambda}_4$	$\mathbf{\Lambda}_5$	$\mathbf{\Lambda}_6$	$\mathbf{\Lambda}_7$	$\mathbf{\Lambda}_8$	$\mathbf{\Lambda}_9$	$\mathbf{\Lambda}_{10}$	$\mathbf{\Lambda}_{11}$	$\mathbf{\Lambda}_{12}$	Π
1.000	0.500	−0.446	0.07114	−0.151	1.035	33.220	0.009781	0.124	0.124	4.149	19.666	19.043	0.268	0.5875

to readapt every 10 generations, leading to the (slightly) non-monotone reduction of the cost function. Often, this action is more efficient than allowing the algorithm not to readapt, since it probes around the current optimum for better local alternatives. Table 1 shows the final design parameters. The entire 1000 generation simulation, with 24 genes per evaluation (24000 total designs) took a few minutes on a laptop, *making it ideal as a design tool.* We note that, for a given set of parameters, a complete simulation takes a fraction of a second, thus thousands of parameter sets can be evaluated in an hour, *without even exploiting the inherent parallelism of the MLA/GA*.

7 Summary and extensions

In summary, Agrophotovoltaic (APV) systems attempt to co-develop the same area of land for both solar photovoltaic power and agriculture. Towards this goal, this work focused developing a computational Digital-Twin framework to track and optimize the flow of optical power through complex multiobjective solar facilities. The optical power flow is rapidly computed with a reduced order model of Maxwell's equations, based on a high-frequency decomposition of optical power into multiple rays, which are propagated forward in time to ascertain multiple reflections and absorption for various system configurations, varying multi-panel inclination, tracking, refractive indices, sizes, shapes, ground refractive properties, etc. The method allows for a solar installation to be tested from multiple source directions quickly and uses a genomic-based Machine-Learning Algorithm to optimize the system. This is particularly useful for planning of complex next-generation solar farm systems involving bifacial (double-sided) panelling, which are capable of capturing ground albedo reflection, exemplified by APV systems. Numerical examples were provided to illustrate the results, with the overall goal being to provide a computational framework to rapidly design and deploy complex APV systems. A key goal of this work was to develop an easy simulation tool that is computationally inexpensive and accessible to a wide range of researchers involved in APV systems. This can accelerate the development of new technologies to maximize agricultural efficiency, quality, safety, water distribution and power management, enabled by computational science and systems engineering. A central component of this framework was the Digital-Twin paradigm of physical reality, i.e. a digital replica of a complex system that can then be inexpensively and safely manipulated, improved and optimized in a virtual setting. The computationally designed system can then be deployed in the physical world afterwards, reducing the potential costs of experiments associated with bringing new technologies to the market. Current work of the author involves incorporating remote sensing imagery and sensor data feeds into the computational framework developed.

Acknowledgements This work has been partially supported by the UC Berkeley College of Engineering and the USDA AI Institute for Next Generation Food Systems (AIFS), USDA award number 2020-67021-32855.

References

1. US National Renewable Energy Laboratory Website (NREL). https://www.energy.gov/science-innovation/energy-sources/renewable-energy/solar
2. Goetzberger A, Zastrow A (1982) On the coexistence of solar-energy conversion and plant cultivation. Int J Solar Energy 1(1):55–69. https://doi.org/10.1080/01425918208909875
3. Harshavardhan D, Pearce Joshua M (2016) The potential of agrivoltaic systems. Renew Sustain Energy Rev 54:299–308. https://doi.org/10.1016/j.rser.2015.10.024
4. Dupraz C, Marrou H, Talbot G, Dufour L, Nogier A, Ferard Y (2011a) Combining solar photovoltaic panels and food crops for optimizing land use: towards new agrivoltaic schemes. Renew Energy 36:2725–2732. https://doi.org/10.1016/j.renene.2011.03.005
5. Liu W, Liu L, Guan G, Zhang F, Li M, Lv H Yao P, Ingenhoff J (2018) A novel agricultural photovoltaic system based on solar spectrum separation. In: Solar energy, vol 162, pp 84–94
6. Malu PR, Sharma US, Pearce JM (2017) Agrivoltaic potential on grape farms in India. Sustain Energy Technol Assess 23:104–110. https://doi.org/10.1016/j.seta.2017.08.004
7. Castellano S (2014) Photovoltaic greenhouses: evaluation of shading effect and its influence on agricultural performances. J Agric Eng 45(4):168–175. https://doi.org/10.4081/jae.2014.433
8. Weselek A, Ehmann A, Zikeli S, Lewandowski I, Schindele S, Hogy P (2019) Agrophotovoltaic systems: applications, challenges, and opportunities. In: A review agronomy for sustainable development, vol 39, Article number: 35
9. Amaducci S, Yin X, Colauzzi M (2018) Agrivoltaic systems to optimise land use for electric energy production. Appl Energy 220:545–561. https://doi.org/10.1016/j.apenergy.2018.03.081
10. Armstrong A, Ostle NJ, Whitaker J (2016) Solar park microclimate and vegetation management effects on grassland carbon cycling. Environ Res Lett. https://doi.org/10.1088/1748-9326/11/7/074016
11. Barron-Gafford GA, Minor RL, Allen NA, Cronin AD, Brooks AE, Pavao-Zuckerman MA (2016) The photovoltaic heat island effect: larger solar power plants increase local temperatures. Sci Rep. https://doi.org/10.1038/srep35070
12. Cossu M, Murgia L, Ledda L, Deligios PA, Sirigu A, Chessa F, Pazzona A (2014) Solar radiation distribution inside a greenhouse with south-oriented photovoltaic roofs and effects on crop productivity. Appl Energy 133:89–100. https://doi.org/10.1016/j.apenergy.2014.07.070
13. Cossu M, Yano A, Li Z, Onoe M, Nakamura H, Matsumoto T, Nakata J (2016) Advances on the semi-transparent modules based on micro solar cells: first integration in a greenhouse system. Appl Energy 162:1042–1051. https://doi.org/10.1016/j.apenergy.2015.11.002
14. Elamri Y, Cheviron B, Lopez J-M, Dejean C, Belaud G (2018) Water budget and crop modelling for agrivoltaic systems: application to irrigated lettuces. Agric Water Manag 208:440–453. https://doi.org/10.1016/j.agwat.2018.07.001

15. Elamri Y, Cheviron B, Mange A, Dejean C, Liron F, Belaud G (2017) Rain concentration and sheltering effect of solar panels on cultivated plots. Hydrol Earth Syst Sci Discuss. https://doi.org/10.5194/hess-2017-418
16. Shiva G, Francesco C, Karunesh Kant Md, Shamim A, Benedetta C, Gholamhassan N, Xingxing Z, Mohammadreza A, Shamshiri Redmond R (2021) A review on opportunities for implementation of solar energy technologies in agricultural greenhouses. J Clean Prod. https://doi.org/10.1016/j.jclepro.2020.124807
17. Homma M, Doi T, Yoshida Y (2016) A field experiment and the simulation on agrivoltaic-systems regarding to rice in a paddy field. J Jpn Soc Energy Resour 37:23-31. https://doi.org/10.24778/jjser.37.6_23
18. Majumdar D, Pasqualetti MJ (2018) Dual use of agricultural land: introducing agrivoltaics in Phoenix metropolitan statistical area, USA. Landsc Urban Plan 170:150–168. https://doi.org/10.1016/j.landurbplan.2017.10.011
19. Marrou H, Dufour L, Wery J (2013a) How does a shelter of solar panels influence water flows in a soil-crop system? Eur J Agron 50:38–51. https://doi.org/10.1016/j.eja.2013.05.004
20. Marrou H, Guilioni L, Dufour L, Dupraz C, Wery J (2013b) Microclimate under agrivoltaic systems: Is crop growth rate affected in the partial shade of solar panels? Agric For Meteorol 177:117–132. https://doi.org/10.1016/j.agrformet.2013.04.012
21. Marrou H, Wery J, Dufour L, Dupraz C (2013c) Productivity and radiation use efficiency of lettuces grown in the partial shade of photovoltaic panels. Eur J Agron 44:54–66. https://doi.org/10.1016/j.eja.2012.08.003
22. Santra P, Pande P, Kumar S, Mishra D, Singh R (2017) Agri-voltaics or solar farming: the concept of integrating solar PV based electricity generation and crop production in a single land use system. Int J Renew Energy Res
23. Trommsdorff T, Kang J, Reise C, Schindele S, Bopp G, Ehmann A, Weselek A, Hogy P, Obergfell T (2021) Combining food and energy production: design of an agrivoltaic system applied in arable and vegetable farming in Germany. Renew Sustain Energy Rev 140:110694. https://www.sciencedirect.com/science/article/pii/S1364032120309783
24. Weselek A, Ehmann A, Zikeli S et al (2019) Agrophotovoltaic systems: applications, challenges, and opportunities. A review. Agron Sustain Dev 39:35. https://doi.org/10.1007/s13593-019-0581-3
25. Valle B, Simonneau T, Sourd F, Pechier P, Hamard P, Frisson T, Ryckewaert M, Christophe A (2017) Increasing the total productivity of a land by combining mobile photovoltaic panels and food crops. Appl Energy 206:1495–1507. https://doi.org/10.1016/j.apenergy.2017.09.113
26. Gross H (2005) Handbook of optical systems. In: Gross H (ed) Fundamental of technical optics, Wiley-VCH
27. Jackson JD (1998) Classical electrodynamics
28. Zohdi TI (2006a) Computation of the coupled thermo-optical scattering properties of random particulate systems. Comput Methods Appl Mech Eng 195:5813–5830
29. Zohdi TI (2006b) On the optical thickness of disordered particulate media. Mech Mater 38:969–981
30. Zohdi TI, Kuypers FA (2006c) Modeling and rapid simulation of multiple red blood cell light scattering. Proc R Soc Interface 3(11):823–831
31. Zohdi TI (2012) Electromagnetic properties of multiphase dielectrics. In: A primer on modeling, theory and computation, Springer
32. Zohdi TI (2015) A computational modeling framework for high-frequency particulate obscurant cloud performance. Int J Eng Sci 89:75–85
33. Zohdi TI (2016) On high-frequency radiation scattering sensitivity to surface roughness in particulate media. Comput Particle Mech. https://doi.org/10.1007/s40571-016-0118-3
34. Zohdi TI (2019) Rapid simulation-based uncertainty quantification of flash-type time-of-flight and Lidar-based body-scanning processes. Comput Methods Appl Mech Eng. https://doi.org/10.1016/j.cma.2019.03.056
35. Holland JH (1975) Adaptation in natural and artificial systems. University of Michigan Press, Ann Arbor
36. Holland JH, Miller JH (1991) Artificial adaptive agents in economic theory (PDF). Am Econ Rev 81(2):365–371
37. Goldberg DE (1989) Genetic algorithms in search, optimization and machine learning. Addison-Wesley, Boston
38. Davis L (1991) Handbook of genetic algorithms, Thompson Computer Press
39. Onwubiko C (2000) Introduction to engineering design optimization. Prentice Hall, Hoboken
40. Goldberg DE, Deb K (2000) Special issue on genetic algorithms. Comput Methods Appl Mech Eng 186(2–4):121–124
41. Zohdi TI (2009) Mechanistic modeling of swarms. Comput Methods Appl Mech Eng 198(21–26):2039–2051
42. Zohdi TI (2018) Multiple UAVs for mapping: a review of basic modeling, simulation and applications. Annu Rev Environ Resour. https://doi.org/10.1146/annurev-environ-102017-025912
43. Zohdi TI (2019) The Game of Drones: rapid agent-based machine-learning models for multi-UAV path planning. Comput Mech. https://doi.org/10.1007/s00466-019-01761-9
44. Zohdi T (2020) A machine-learning framework for rapid adaptive digital-twin based fire-propagation simulation in complex environments. Comput Methods Appl Mech Eng. https://doi.org/10.1016/j.cma.2020.112907
45. Luenberger D (1974) Introduction to linear and nonlinear programming. Addison-Wesley, Menlo Park
46. Gill P, Murray W, Wright M (1995) Practical optimization. Academic Press, New York